



Role of TiB₂ inoculation particles during welding of a AlCoCrFeNi high entropy alloy



J.G. Lopes ^{a,*}, A. Candeias ^e, P. Agrawal ^{b,c}, J. Shen ^e, N. Schell ^d, R.S. Mishra ^{b,c}, J.P. Oliveira ^{e,*}

^a UNIDEMI, Department of Mechanical and Industrial Engineering, NOVA School of Science and Technology, Universidade NOVA de Lisboa, Caparica 2829-516, Portugal

^b Center for Friction Stir Processing, Department of Materials Science and Engineering, University of North Texas, Denton, TX 76207, USA

^c Advanced Materials and Manufacturing Processes Institute, University of North Texas, Denton, TX 76207, USA

^d Institute of Materials Physics, Helmholtz-Zentrum Hereon, Max-Planck-Str. 1, Geesthacht D21502, Germany

^e CENIMAT/I3N, Department of Materials Science, NOVA School of Science and Technology, Universidade NOVA de Lisboa, Caparica 2829-516, Portugal

ARTICLE INFO

Keywords:

High entropy alloys
Gas tungsten arc welding
Synchrotron X-ray diffraction
Microstructure
Mechanical testing
Thermodynamic simulations, Inoculants

ABSTRACT

High entropy alloys (HEAs) are a novel class of materials that represent an evolution of common engineering alloys to a wider array of compositional and properties possibilities. As such, the exploration of methodologies to achieve improved microstructure and mechanical characteristics of these materials for potential applications in industry is a requirement that is experiencing extended research efforts. One example of a processing method able to expand the potential applications of these alloys is Gas Tungsten Arc Welding (GTAW), which allows to evaluate the metallurgical evolution and corresponding mechanical performance, associated to the impact of a localized heat input on the material. However, GTAW and related fusion-based welding processes are known to generate large grain sized-structures in the fusion zone, which often is detrimental to the joint performance. Thus, the integration of high temperature inoculant particles on the fusion zone during welding is a potential way to improve this region's microstructure and, therefore, its mechanical performance. In this work, we discuss the effect that the addition of TiB₂ micron-sized particles have on the microstructure of a GTAW AlCoCrFeNi-based HEA. For this, the microstructure of the welds was evaluated by means of optical and electron microscopy, synchrotron X-ray diffraction and CalPhaD-based simulations. Mechanical testing was performed using micro-hardness mapping and tensile testing coupled with digital image correlation. The results evidenced that successful inoculation with TiB₂ proved capable of altering the microstructure of the fusion zone (FZ), refining it. Nevertheless, preferential deformation in the relatively softer heat affected zone during tensile testing resulted on premature failure of the inoculated joints, due to the concomitant higher hardness of the FZ.

1. Introduction

With the most recent industrial and scientific advancements, a new class of materials, high entropy alloys (HEAs), has been developed. These materials are continuously under research to improve their potential applicability in an industrial setting. HEAs are characterized by being composed of multiple principal elements, which allows for a wider array of compositional possibilities and consequently allows tailoring its mechanical performance, through compositional adjustments.

Of especial emphasis in this class of alloys, is the AlCoCrFeNi HEA system which has been the focus of several successful attempts to improve its properties, namely mechanical performance and resistance to corrosive and/or high/low temperature environments [1–4]. The

process of achieving an HEA with such desired capabilities, however, requires a thorough investigation of its characteristics under different conditions since these alloys will eventually be required to sustain different manufacturing processes until a final product is obtained.

Welding is a widely used and accepted processing method that allows to generate permanent bonds on monolithic parts, enabling the creation of complex structures. While welding has been used with multiple metallic alloys targeting structural applications in various industrial sectors [5,6], the metallurgical evolution induced by the welded thermal cycle is a fundamental topic to be considered since it will condition the mechanical and eventual functional response of the joint. Moreover, the rapid, non-equilibrium thermal cycle during fusion-based welding can give rise to heterogenous and metastable phase structures with potential

* Corresponding authors.

E-mail addresses: jcg.lopes@campus.fct.unl.pt (J.G. Lopes), jp.oliveira@fct.unl.pt (J.P. Oliveira).

critical implications in the adoption of the processed material in different industries.

Welding offers a wide array of different processes that can be used to obtain excellent mechanical properties on the resulting joints. In the case of fusion-based welding, the material will locally experience high temperatures overcoming its melting point, which is followed by a subsequent solidification that often leads to microstructure features significantly different from those of the original base material (BM). Moreover, adjacent to the fusion zone (FZ), the high temperatures experienced, although below the material melting point, can promote solid state transformations that will also impact the local mechanical response. This region corresponds to the heat affected zone (HAZ). Beyond this, it is not guaranteed that the performance of the welded joint outperforms the behavior of the non-processed BM. In fact, that is not often the case, since unwanted microstructures can form in both the HAZ and FZ. These unwanted microstructures include large and highly oriented grains, which tend to decrease the joint strength and promote an anisotropic behavior at these locations. A way to mitigate excessive grain growth in the FZ is via the introduction of high temperature solid particles, which will act as inoculants and promote significant grain refinement, provided they remain in the solid state during the local melting experienced by the material [7–9].

Existing literature evidences that TiB_2 stands as a good candidate to improve the mechanical performance of welded joints when used as inoculant, as evidenced by different research works focusing on Al-based alloys [10–13], steels [14,15], Ni-based superalloys [16,17] and even HEAs [18,19].

Gas Tungsten Arc Welding (GTAW) is known for its relatively low cost when compared to other welding techniques, such as laser and electron beam welding, and has wide availability in industry [20]. As such, the present work assesses how the introduction of TiB_2 particles on the molten pool of a AlCoCrFeNi HEA during GTAW affects the joint microstructure and mechanical response. Welding of this HEA system was already successfully attempted before [21], although the impact of inoculants introduction is yet unknown. Through the use of multiscale characterization techniques, namely optical and electron microscopy, high energy X-ray diffraction and mechanical testing, at both micro and macroscales, the microstructure and property evolution are detailed. Thermodynamic calculations aid in rationalizing the impact of the TiB_2 inoculant particles on the GTAW joints.

2. Materials and methods

In this work, 1.5 mm slates of an as-cast AlCoCrFeNi HEA system, with a nominal composition of 16.4 Al, 16.4 Co, 16.4 Cr, 16.4 Fe and 34.4 Ni (all values in at%), were used as the BM for GTAW.

Prior to welding, the as-received material was coated with a mixture of ethanol and commercially available TiB_2 powder, with a particle size ranging between 5 and 8 μm . The plate was then left to dry until the ethanol mixture evaporated. After, GTAW was performed on the TiB_2 -coated and uncoated BMs, to assess the impact of these inoculant particles on the FZ microstructure and resultant joint properties. The welding parameters comprised a current intensity of 100 A, a torch speed of 60 mm/min and a constant electrode-to-sample distance of 1.5 mm. Commercially pure Argon (99.999% purity) was utilized as the shielding gas, being applied at a flow of 8 and 5 L/min on the face and root of the welded joints, respectively.

Following welding, conventional metallographic preparation methods were used, where the cross sections of both types of samples were polished from 600 grit sandpaper to 3 μm diamond paste, and finally etched with aqua regia solution (in a ratio of 1:3 of nitric acid and hydrochloric acid, respectively) to reveal the microstructure characteristics.

Optical microscopy was performed using a Leica DMI5000 M inverted microscope. Scanning electron microscopy (SEM) imaging, energy dispersive X-ray spectroscopy (EDS) and electron backscatter

diffraction (EBSD) were also performed using a FEI Nova NanoSEM 230 equipped with EDAX Hikari Super EBSD.

Synchrotron X-ray diffraction was performed at the P07B beamline at Petra III in DESY, Germany, to determine the existing phases across the different regions of the joints. The setup involved working in transmission mode, with an incoming X-ray beam with a wavelength of 0.14235 Å. The joint was probed using a beam size of 500 \times 500 μm , with a 500 μm spacing between each scan. Scanning was performed from one side of the BM, going through the FZ and finishing on the opposite side of the BM.

To understand the effect of the TiB_2 particles on the molten pool solidification path, thermodynamic calculations were performed using Thermo-Calc software. The TCHEA 5.1 database was used.

Microhardness mapping was performed in a Mitutoyo Micro Hardness Testing Machine HM-112, with a load of 0.5 Kg applied during 10 s. Multiple indentations were then executed covering the joint cross section, with a 150 μm spacing between each indentation in both the longitudinal and transverse directions.

To investigate the tensile properties exhibited by the inoculated and non-inoculated samples, tensile testing was performed using an autograph Shimadzu AG50kNG machine with a 50 kN load cell equipped. The tensile force was applied perpendicularly to the welding direction at a displacement rate of 1 mm/min, while digital image correlation (DIC) data was recorded using an in-house developed apparatus. The resulting fracture samples were then observed using SEM.

3. Results and discussion

In this work, GTAW was performed with and without the addition of TiB_2 particles on the AlCoCrFeNi HEA system. In this section we delve into the microstructural characterization on both types of samples, highlighting the differences between the inoculated and non-inoculated conditions, and establish a proper understanding of the microstructure of both joints, making it possible to correlate these with their corresponding mechanical performance.

This initial section is divided into four subsections. The first starts to introduce the welded joints at the macroscopic level, highlighting their differences and in the following sections we particularize the discussion to the regions of interest characteristic of these joints, namely the BM (used as benchmark), HAZ and FZ. This will make it possible to unveil the microstructure evolution and correlate it with the joint thermal cycle and/or with the addition of the TiB_2 particles.

3.1. Macroscopic overview of the welded joints

Fig. 1 displays the macrostructure of the welded joints in the non-inoculated (a) and TiB_2 -inoculated conditions (c), allowing to detail the microstructural changes induced by the presence TiB_2 on the molten pool during welding. Additionally, electron backscattered diffraction (EBSD) images quality index (QI) maps overlayed with inverse pole figure (IPF) maps are also displayed for each type of sample (**Fig. 1b** and d, respectively).

It is possible to observe that there is a distinct morphology of the FZ in both samples although the welding parameters used for both conditions were kept the same. These differences in weld shape resulted from the alteration of the electric arc conditions due to the introduction of the TiB_2 particles on the material top surface. That is, due to its good electrical and thermal conductivity [22,23], the TiB_2 layer aided in the conduction of the electric current to the material, allowing the same amount of heat input to be supplied to the joint in a more restricted area, thus increasing the energy density associated to the process. Since the inoculant particles have a higher thermal conductivity, there will be a more pronounced energy transfer to the BM, which aids in increasing the dimension of the FZ. These combined effects alter the weld thermal cycle and extend the length and geometry of the FZ. In fact, the shape of the FZ changed from \approx 4.7 mm in the face and \approx 3.1 mm in the root of the weld,

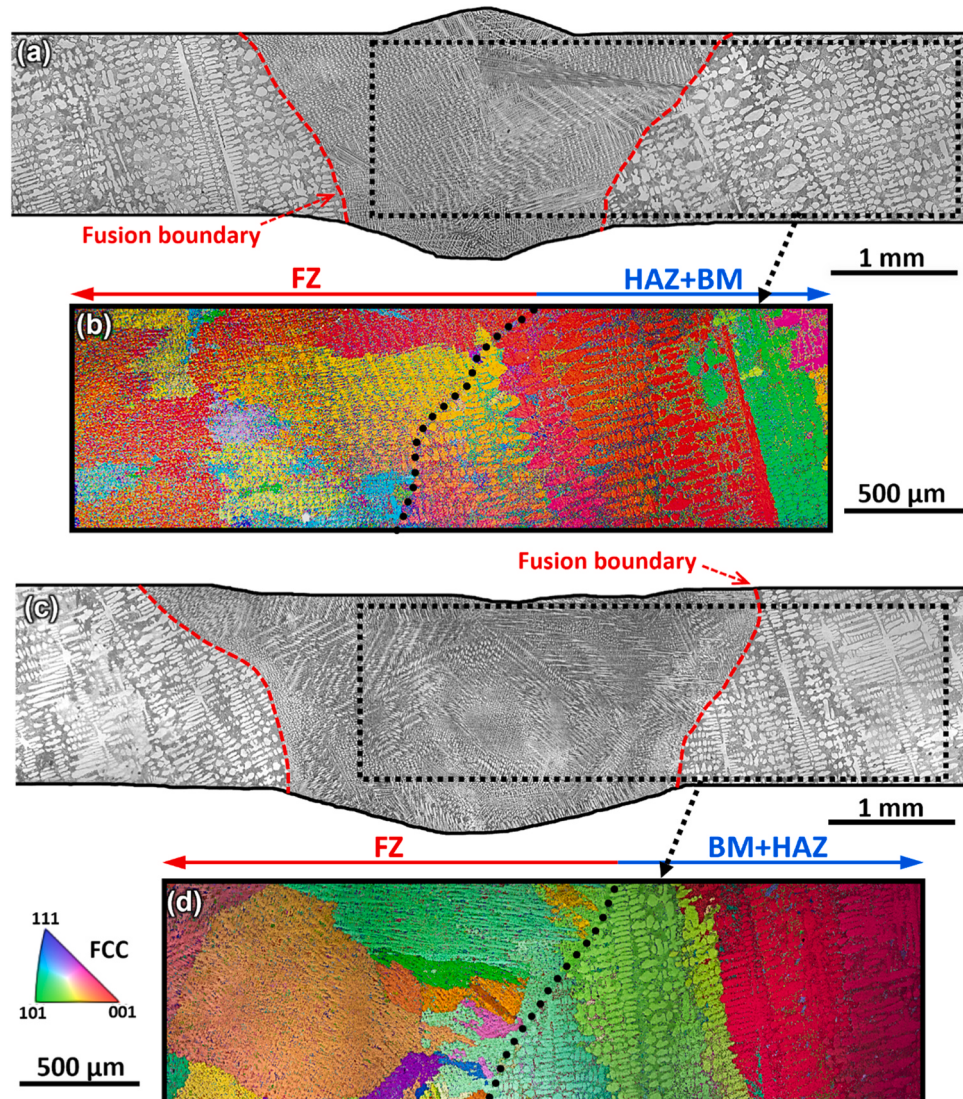


Fig. 1. - Macrostructure of the GTAW AlCoCrFeNi HEA joints: (a) and (c) correspond to the optical micrographs of the non-inoculated and inoculated joints, respectively, while (b) and (d) comprise the superposition of the EBSD IQ map of the IPF map and the non-inoculated and inoculated materials, respectively.

in the non-inoculated case, to a joint with a face width of ≈ 3.7 mm and a root width of ≈ 2 mm for the inoculated samples.

Microstructure differences that arise from the distinct weld thermal cycle in the heat affected zone (HAZ) are not easily identifiable due to the dendritic nature of the BM microstructure. This is related to the previous processing of the original BM where the relatively slow cooling upon casting will delay eventual solid-state transformation to occur in the HAZ of the present joints during welding.

For improved visualization of the joint macrostructure, Fig. 1b) and c) displays low magnification EBSD maps. It can be observed that for the non-inoculated samples there is an increased tendency for the FZ grains to exhibit a red coloration indicating a preferred texture along the $<001>$ direction, this being the easy growth direction of FCC materials. In the inoculated joint, the developed texture is not so strong. This can be ascertained to the heterogeneous nucleation promoted by the TiB₂ particles. It can be observed that, although the microstructural differences are evident, the FZ grains also indicate that growth in other directions also occurred, resulting from the effect of the introduction of inoculants in the molten pool.

With the overall perspective on the welded joints established, the following sections will discuss the microstructural differences present in both welds. Firstly, attention will be given to the initial condition of the

BM followed by the analysis of fusion boundary (FB), finally the discussion of the microstructural features comprising the FZ will be analyzed. Further advanced characterization methods of the welded joints will also be provided alongside their mechanical characterization.

3.1.1. Description of the AlCoCrFeNi HEA base material

To ensure the structural integrity of the obtained joints, it is crucial to evaluate their microstructure at a higher resolution scale. Fig. 2 illustrates the initial condition of the AlCoCrFeNi HEA BM used in this study. As can be observed from Fig. 2(a), although the present base material came from the same ingot as in [21], where a fully eutectic FCC (white regions) + B2 BCC (black regions) microstructure was observed, here, a primary FCC phase followed by the eutectic FCC + B2 BCC constituent is observed, highlighting a phase structure offset regarding the nominal eutectic composition of the BM.

Such offset can be explained by the cooling conditions experienced by different regions of the ingot, which were left to cool slowly until reaching room temperature. These conditions can provide the means for the formation of a higher amount of primary FCC phase. That is, the cooling rate at which the liquid and subsequently the solid material experiences, affects the time available for diffusion between the solid and liquid phases. Depending on the region of the ingot, different

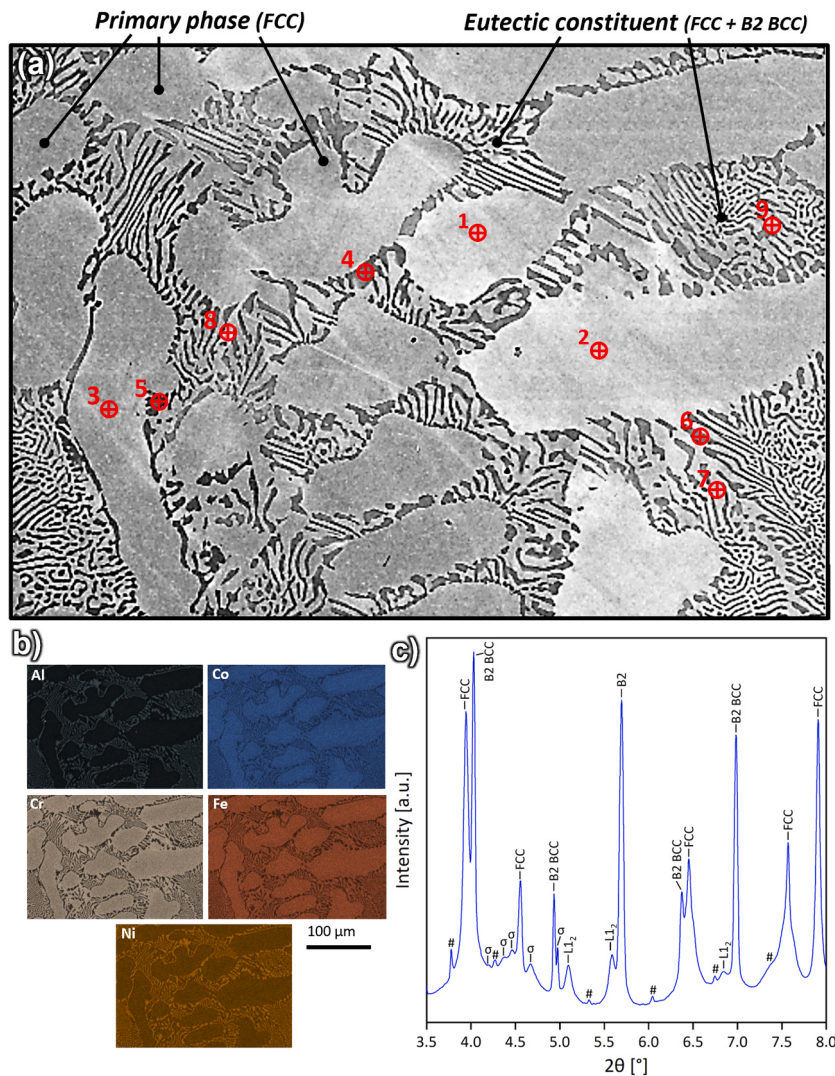


Fig. 2. – (a) Initial condition of the AlCoCrFeNi HEA BM showcasing large primary FCC grains and the eutectic (FCC + B2 BCC) constituents observed by SEM and (b) corresponding EDS maps. The points marked in (a) correspond to the EDS point analysis results exhibited in Table 2. In (c) a representative synchrotron X-ray diffraction pattern indicates the presence of more (nanometric) phases in the BM.

locations experience distinct cooling conditions, potentially giving rise to a heterogeneous structure along the ingot. Moreover, faster cooling rates can yield a more uniform eutectic microstructure, while slower cooling can result in the formation of larger grains, compounded by the possible deviation of the liquid composition a solute rich/poor state (depending on the elemental availability and phases developed).

The clear depiction of the microstructural features of the BM was obtained by SEM (refer to Fig. 2). Here the distinction between the primary FCC phase and eutectic FCC + B2 BCC constituents are compared in terms of their elemental distribution using energy-dispersive X-ray spectroscopy (EDS). From these EDS measurements (refer to Fig. 2(b)), it can be qualitatively observed that the FCC phase has a higher amount of Cr, Co and Fe, while the B2 BCC phase is richer in

both Al and Ni.

Quantification of the composition of the BM is displayed in Table 1. Here it is possible to observe that deviation of the nominal composition occurred, highlighting the non-uniform condition of the ingot from where the plates prior to welding were obtained. For comparison, the composition obtained in the BM in [21], which came from the same ingot, is also presented.

Comparing the BM (from this study) with the nominal composition of the eutectic condition of the alloy, it can be perceived that the Al, Co and Ni content is reduced in 0.4, 0.3 and 1.6 at%, respectively. Conversely, the amount of Cr and Fe is increased, with Cr presenting the highest variation from the nominal composition of the HEA (nearly 1.6 at%). Such allows us to infer upon the microstructure that formed during solidification of this region of the ingot. The elemental deviation from the nominal composition indicates that the FCC phase has higher propensity to form at higher temperatures, while the B2 BCC phase requires the appropriate conditions to form as part of the eutectic structure. Such can be expected from the preferential elemental enrichment of each phase. This can occur due to the large availability of the components that tend to ease the nucleation of the Co, Cr, and Fe-rich FCC phase, while the scarcer Al and Ni combination required for the nucleation of the B2 BCC phase is only attained when the necessary temperatures and elemental

Table 1 –
Compositional comparison of the AlCoCrFeNi HEA base material.

	Composition (at%)				
	Al	Co	Cr	Fe	Ni
Nominal composition	16.4	16.4	16.4	16.4	34.4
BM (from [21])	11.2	13.0	15.7	18.2	41.9
BM [present study]	16.0	16.1	18.0	17.1	32.8

proportions for the B2 BCC phase formation are reached [21,24].

Further quantification of the site-specific phases on the BM marked on Fig. 2(a) can be found in Table 2. There, we can observe that the composition of the large FCC grains (which formed first during solidification) is different from the composition of the FCC phase within the eutectic constituent. This attests to the high entropy effect characteristic of these novel metals that are capable of forming a crystal structure from a wide variety of atoms. The same can be said for the B2 BCC phase.

Microscopy techniques only yield information at the surface level of the material. To unveil the bulk microstructural condition, it is necessary to resort to other advanced characterization techniques. Synchrotron X-ray diffraction was performed on the BM of the AlCoCrFeNi, with the associated diffraction pattern being shown in Fig. 2(c). The diffraction data reveals the presence of more phases on the microstructure other than the FCC and B2 BCC phases previously identified by optical and electron microscopy. In fact, it is possible to identify diffraction peaks corresponding to sigma (σ) and $L1_2$ FCC phases as well. Such results are compliant with what is expected from the literature regarding this HEA [25–28] and may result from elemental segregation under the solidification conditions taken by this portion of the ingot during its manufacturing, as well as minor material contamination of the raw material used to cast the BM.

Considering the abovementioned compositional differences and the phases encountered via X-ray diffraction, thermodynamic calculations were used to generate an equilibrium phase diagram of composition (nominal and real) as function of Cr (the element with the most deviation from the nominal composition). These results are depicted in Fig. 3.

Clearly, the different compositions result in distinct conditions for phase nucleation during solidification. A shift on the eutectic point can also be observed going from 16.8 to 18.4 at% of Cr. Equilibrium conditions are based in ideal cooling conditions, which are very difficult to occur in actual thermomechanical processes, such as casting and welding. Nevertheless, according to the equilibrium and Scheil solidification curves of Fig. 3 it is possible to expect the formation of B2 BCC and FCC phases, thus in good agreement with the previously shown characterization data (microscopy and X-ray diffraction). The only variation between the Scheil calculation data resides in the temperature at which the liquid starts to solidify, where a minor difference of $\approx 3^\circ\text{C}$ is noticeable between them.

As such, considering the nominal composition of the HEA, it is possible to infer that the FCC phase starts to solidify in a first stage until reaching the point where the FCC and the B2 BCC phases appear simultaneously within the Liquid phase as a eutectic reaction. At this point, both the B2 BCC and FCC phases start to nucleate from the interdendritic fluid that remained in the liquid state [29]. Such explains why it is possible to observe large FCC grains in the BM ranging from smaller to larger dendrites ($52 \pm 20 \mu\text{m}$ vs $649 \pm 195 \mu\text{m}$, respectively), while in the eutectic domain their size is considerably smaller, with the interdendritic distance between them being $2.7 \pm 0.5 \mu\text{m}$.

3.1.2. Clarifying microstructural differences at the FB of both welded joints

To further evaluate the impact of the welding process on the material

Table 2

– EDS single point analysis results. The scanned regions are marked in Fig. 2(a).

Location	Phase	Point	Composition (at%)				
			Al	Co	Cr	Fe	Ni
Large grains	FCC	1	13.1	16.9	22.8	19.0	28.2
		2	11.6	18.4	23.9	20.8	25.2
		3	11.7	20.8	18.5	20.2	28.8
Eutectic constituent	B2 BCC	4	12.9	18.2	19.5	18.6	30.7
		5	10.7	15.7	21.1	21.7	30.8
		6	15.6	18.4	21.1	26.4	27.5
Eutectic constituent	FCC	7	29.9	9.5	11.0	13.3	36.3
		8	23.8	13.4	13.0	17.3	32.4
		9	25.0	13.0	15.2	19.4	27.5

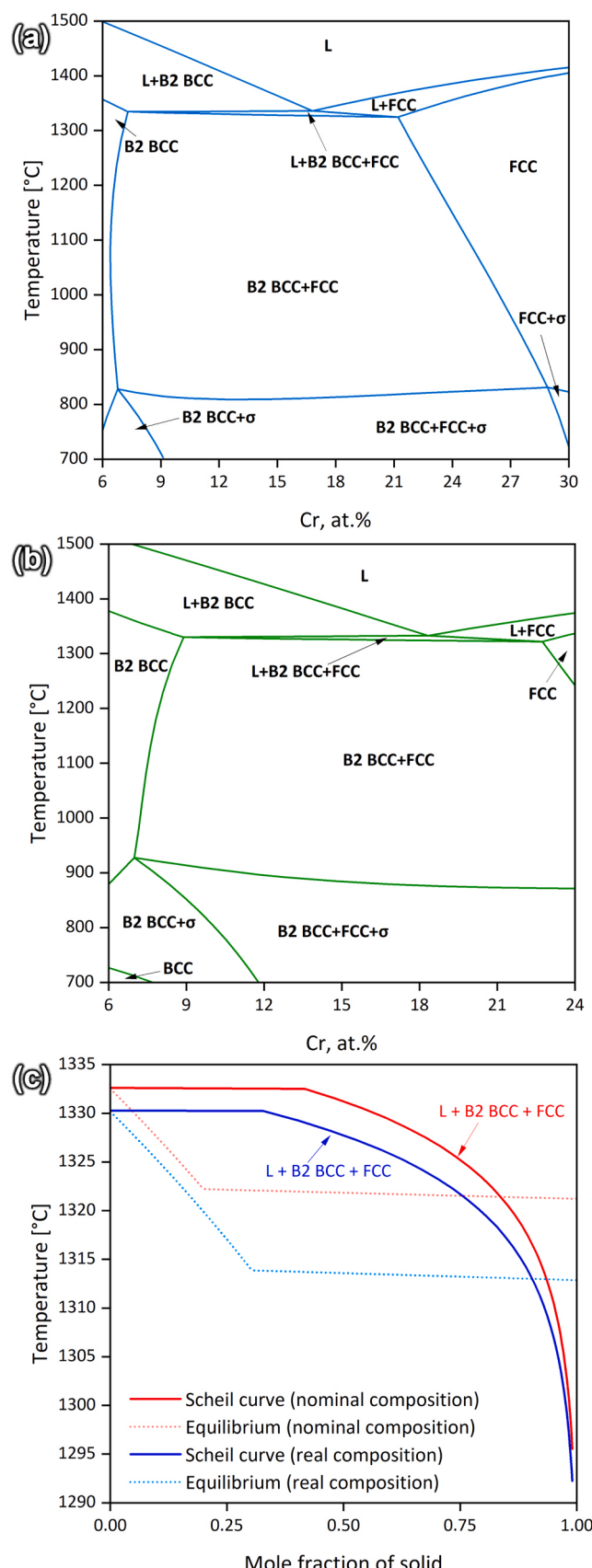


Fig. 3. – Phase diagrams calculated considering: a) nominal composition and b) real composition (L stands for Liquid phase). The Scheil solidification curves of both compositions are shown in c).

microstructure, attention is now devoted to the FB. This region comprises both the microstructural condition of the HAZ and its frontier with the FZ. Again, due to the dendritic microstructure that developed during casting of the HEA BM, distinguishing the HAZ from the BM proves to be difficult using solely microscopy techniques. Since the heat input for both types of joints, i.e., inoculated and non-inoculated conditions, is similar, changes between both the HAZ are expected to be minimal. With this into account, Fig. 4 displays a representative synchrotron X-ray diffraction pattern taken from the HAZ, allowing to identify the phase structure at this location. The HAZ displays a different microstructural condition than that of the BM, as the presence of low intensity peaks corresponding to σ and L_1_2 FCC phases are almost non-existent, suggesting a decrease in the phase volume fraction of both phases. This can be explained based on imposition of a localized heat treatment owing to the weld thermal cycle, which will promote phase dissolution (partial or full, depending on the distance to the heat source). Regarding this, considering the compositions between the nominal and effective composition (refer to Fig. 3), it is expected that regions of the joint reaching $\approx 1300^{\circ}\text{C}$ develop FCC and B2 BCC phases within its microstructure upon solidification. At the same time, regions of the welded joint attaining temperatures within the $800\text{--}900^{\circ}\text{C}$ range are expected to become enriched with σ phase. As such, diffraction peaks corresponding to the FCC, B2 BCC and σ phases can be observed in the HAZ (refer to Fig. 4), which is in line with the optical and electron microscopy observations previously shown in Fig. 1 and Fig. 2.

In opposition to the HAZ, the FZ on both samples exhibits evident microstructural differences. To evaluate the changes induced in the FZ by the introduction of TiB_2 particles, and compare them with the non-inoculated condition, high magnification optical images of the FB of both welded joints are depicted in Fig. 5.

Starting with the non-inoculated sample, shown in Fig. 5(a), the transition from the HAZ to the BM evidences a steep variation between the large dendrites comprising the primary FCC and the FCC + B2 BCC eutectic microstructure in their midst (similarly to the BM) and smaller equiaxed dendritic structures that are formed within the FZ boundaries. Without the addition of TiB_2 , the microstructure of the FZ, tends to exhibit equiaxed FCC dendrites surrounded by the FCC + B2 BCC eutectic constituents within the interdendritic space. Here, as observed,

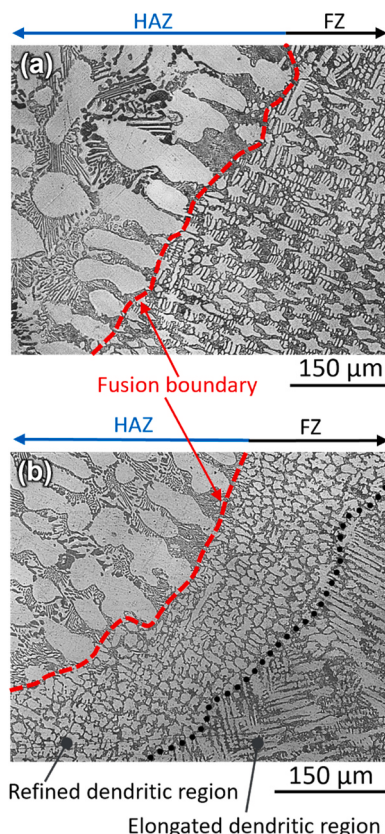


Fig. 5. – Detailed optical micrograph view of the microstructure features at the HAZ/FZ boundary: (a) fusion boundary of the non-inoculated joints and (b) fusion boundary of the TiB_2 inoculated samples.

major changes in microstructure of the FZ occur on the grain size and morphology, where there is a refinement compounded by a change in morphology from large columnar grains in the BM to equiaxed dendritic ones in the FZ, indicating the impact of the cooling rate on the solidification structure. In fact, the cooling rate of the FZ is higher than that experienced by the material during casting, thus justifying the morphological differences observed.

A different microstructural condition at the FB is found when the TiB_2 inoculants are added during GTAW (refer to Fig. 5b)). In this case, beyond the solidification parameters, namely temperature gradient (G) and the growth rate (R), that reign over the size and morphology of the microstructural features developed in the non-inoculated welded joints, the introduction of TiB_2 on the FZ allows for the intensification of heterogeneous nucleation [30], as these high temperature solid particles aided in the generation of more nuclei which can then evolve to grains. This adds another factor, beyond the cooling rate, that significantly influences the developed solidification structures in the inoculated FZ microstructure.

Here, the FZ of the inoculated material exhibits refined equiaxed grains closer to the fusion boundary, whereas when going towards the bulk of the FZ, small columnar dendrites (reaching $\approx 80 \mu\text{m}$ of length) grow perpendicularly to the FB towards the bulk of the FZ. This shows that the molten pool's solidification conditions changed to the extent that the structures formed upon cooling deviated from the expected microstructural characteristics of the non-inoculated samples, namely the equiaxed FCC dendrites surrounded by FCC + B2 BCC constituents. The refined dendritic region evident at the FB, is often referred to as a fine equiaxed zone (FQZ) in the literature [31–33]. Beyond the fast cooling due to the heat sink effect caused by the proximity to the BM, its formation can be associated with heterogeneous nucleation, which in the present case can be induced by the TiB_2 particles.

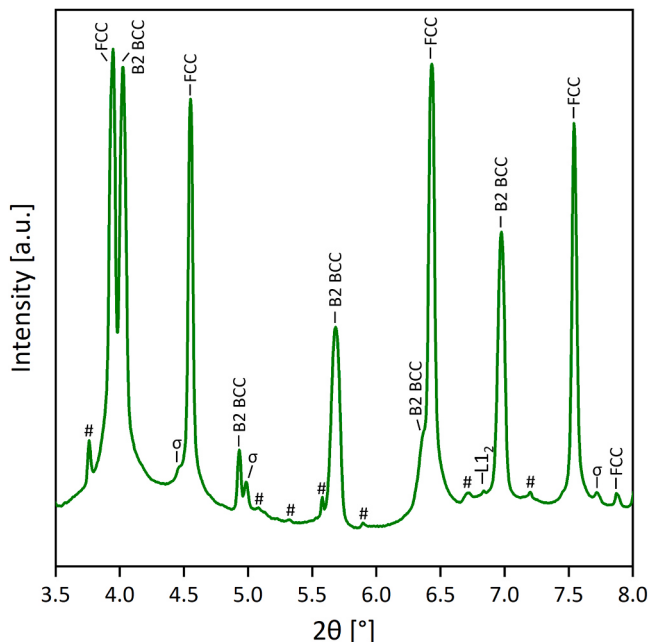


Fig. 4. – Representative synchrotron X-ray diffraction pattern from the HAZ. (# stands for the low intensity 2nd harmonic diffraction peaks that do not correspond to any structure present on the alloy).

Nonetheless, other factors such as welding parameters and fluid flow conditions along the torch path also contribute to its formation and extension. However, since the major difference between the two conditions is the presence of the TiB_2 particles, it can be stated that these particles are the fundamental factor promoting this heterogeneous nucleation phenomena. It should be mentioned that the presence of the FZ in the microstructure can be detrimental to the mechanical properties by contributing to appearance of a complex stress state of the joint, being this location a region where weld defects, such as microcracks, are prone to occur, since this region is often characterized by its poor intergranular strength, leading to a weak resistance to cracking during mechanical solicitation [31].

From the analysis of the FB, it can be concluded that a different microstructural condition is clearly identifiable near the transition between the HAZ to the FZ. Nevertheless, most changes due to the introduction of the TiB_2 in the molten pool are visible in the bulk of the FZ, which is discussed in the next section.

3.1.3. Bulk fusion zone evolution in inoculated and non-inoculated samples

The microstructure features present at the bulk of the FZ on both inoculated and non-inoculated conditions are presented in Fig. 6, alongside with the corresponding IPF EBSD maps. As mentioned previously, the microstructure of the non-inoculated sample is comprised mostly of large equiaxial dendritic FCC grains surrounded by the eutectic constituents, FCC + B2 BCC phases. The same, however, does not occur on the TiB_2 -inoculated sample where an nonexistent uniformity of grain structures is present, ranging from small refined equiaxial grains to columnar dendritic structures distributed amidst the microstructure. To understand these differences, it is important to comprehend how the addition of TiB_2 can affect the solidification conditions of the molten pool, namely what occurs during the welding process that can modify the G and R values to the point of achieving such differences in the FZ.

Given the high melting point of TiB_2 (2790 °C, from [34]), heterogeneous nucleation is intensified in the presence of these solid particles in the melt pool, effectively reducing the energy barrier for grain

nucleation to occur. This allows for new grains to start developing at the TiB_2 particles interfaces, as these inoculants may not dissolve completely due to their size (5–8 μm) and the temperature distribution attained on the molten pool. Such phenomenon differs from epitaxial growth, where grains nucleate from the solid material present at the fusion boundary, where the temperature of the FZ is at its lowest. The introduction of inoculants can, therefore, promote the development of a finer grain structure, as evidenced by the direct comparison of both FZ.

However, GTAW is known for being able to reach temperatures as high as 20000 °C in the electric arc [30,35]. Due to the extremely high temperature that can develop in the FZ of GTAW joints, there is the possibility for (partial) dissolution of the high temperature TiB_2 particles. This will promote changes in the chemical composition of the FZ and can alter the melting point of the liquid material, and thus also modify the conditions for which heterogenous nucleation may occur within the FZ [29,30].

Another difference that can be observed within the FZ is the presence of larger FCC equiaxial dendrites in the non-inoculated joint. In the inoculated sample the equiaxial FCC dendrites exhibit an average size of $38.1 \pm 23.1 \mu\text{m}$, with the FCC interdendritic spacing achieving maximum values of $4.6 \pm 1.8 \mu\text{m}$, which contrasts with the $31.1 \pm 17.9 \mu\text{m}$ and $10.9 \pm 5.5 \mu\text{m}$ respectively measured on the larger FCC grains, for the non-inoculated condition. In the case of the TiB_2 -inoculated samples, however, we can observe the presence of larger grains amidst smaller sized ones. This phenomenon can be attributed to the uneven distribution and dissolution of the TiB_2 particles during melting, which can effectively alter their dispersion along the FZ, although the thickness of the samples is relatively small (1.5 mm). Furthermore, evidence of eutectic-like morphologies within the microstructure can also be observed although being scarcer (see Fig. 6(d)). These are a product of the uneven elemental distribution occurring during solidification in the inoculated samples.

Fig. 7 details EDS data revealing the elemental distribution on the FZ of both the inoculated and non-inoculated samples. Considering the non-inoculated FZ, using elemental maps and following the corresponding

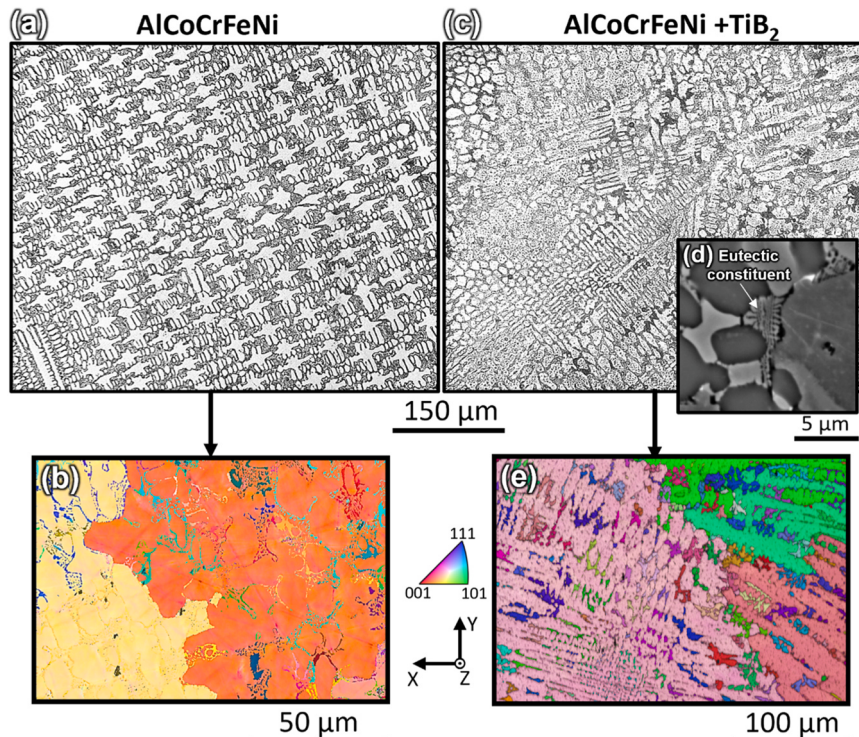


Fig. 6. – Microstructural differences between both types of samples: (a) optical microscopy and (b) EBSD of the non-inoculated samples; (c) optical microscopy, detailed view of the eutectic constituent (d) and (e) EBSD of the TiB_2 inoculated samples.

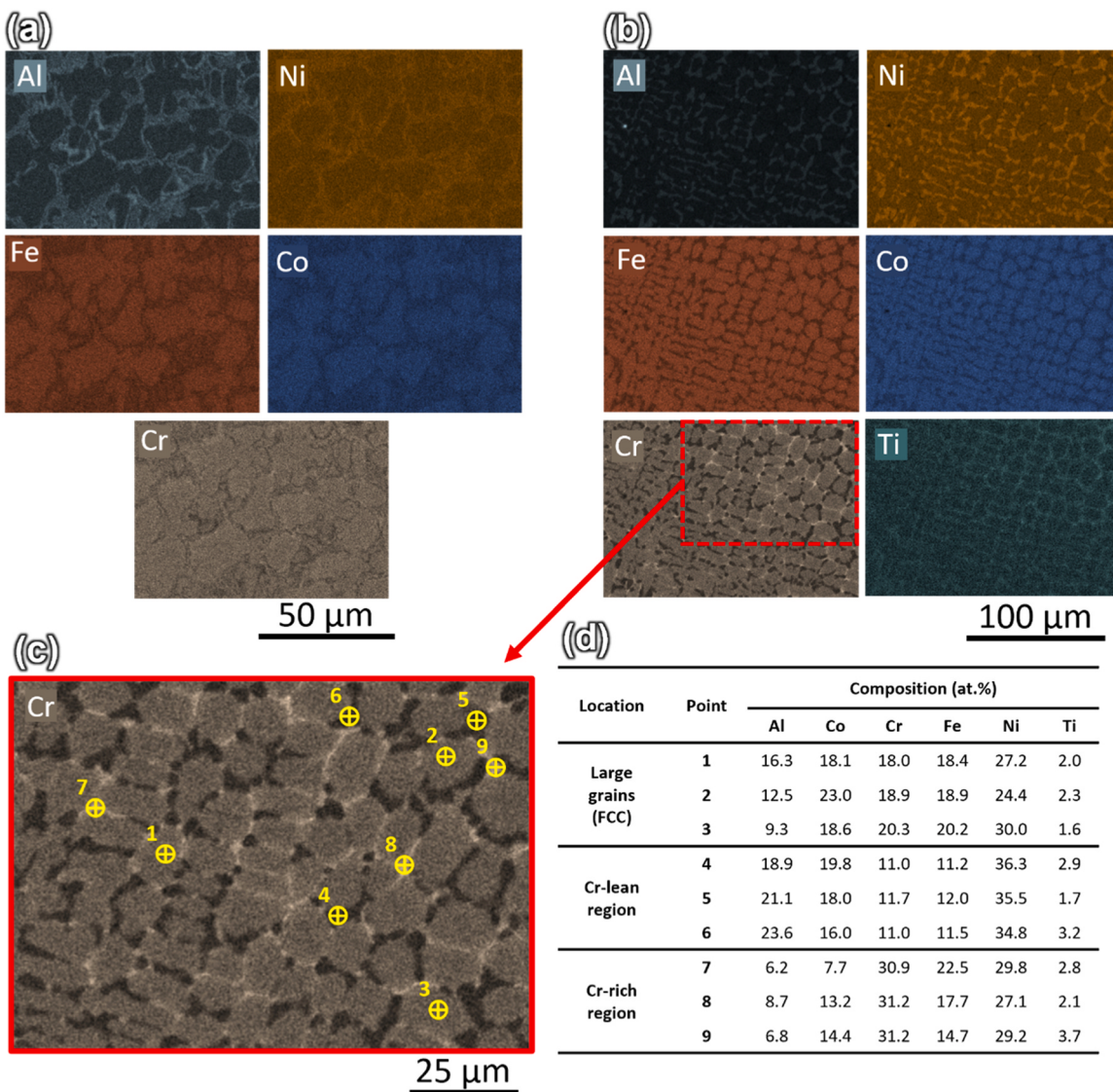


Fig. 7. – EDS maps of non-inoculated (a) and inoculated (b) joints. For b) a Ti map was added to track the changes induced in the FZ composition due to partial dissolution of the TiB_2 particles. A detailed view of the Cr map of the inoculated FZ is displayed in (c) marking the points where EDS scans were performed. The EDS point results are shown in (d).

phase diagram, the first phase being formed is the FCC phase. Such is compliant with the obtained microstructure. As expected from the data retrieved from the BM, this phase is mainly composed of Cr, Co and Fe. Additionally, as the FCC phase forms and the temperature decreases the B2 BCC phase becomes stable, being richer in Al and Ni and forming the eutectic constituent within the larger FCC grains.

However, on the TiB_2 -inoculated sample the EDS maps revealed that the FZ had an averaged composition of 14.9% of Al, 16.2% of Co, 18.1% of Cr, 17.3% of Fe, 32.8% of Ni and 0.7% of Ti (contrasting to the approximately 10% of Al, 17% of Co, 24% of Cr, 19% of Fe, 29% of Ni measured in the non-inoculated condition). No evidence of Boron was observed due to its low atomic weight and fraction. Interestingly, another difference occurring between both cases is in the Al, Ni and Cr content. While the presence of the FCC and B2 BCC phases is still clear, some regions hint for the formation of a different phase within the microstructure which possesses a high amount of Cr and being practically depleted of Al and Ni.

EDS point quantification of the inoculated FZ composition can be observed in Fig. 7(c) and (d). Interestingly, the presence of BCC Cr-rich precipitates amidst the B2 BCC phase was evidenced by Miao et al. [36], indicating that the conditions for the formation of this phase can be

fulfilled as segregation of Al, Ti, Cr and Ni occurs. However, these regions also evidence the presence of Co and Fe, beyond the high amount of Cr, indicating the possibility for σ phase formation [37,38].

Given this, the elemental distribution observed in the EDS maps of Fig. 7, it is possible to further infer upon solute redistribution during solidification and subsequent phase nucleation using a CalPhiD-based analysis. As such, considering the non-equilibrium solidification conditions generated during cooling of the molten pool due to the GTAW process, Scheil calculations were performed as shown in Fig. 8(a).

As expected, the Scheil-Gulliver curves of both conditions display several differences between them (refer to Fig. 3(c)). While the non-inoculated sample only shows a direct nucleation of B2 BCC and FCC from the Liquid phase, the inoculated sample exhibits two solidification steps. Taking this into consideration, the first step consists of the formation of FCC phase from the Liquid. Subsequently, it experiences the nucleation of a BCC and a B2 BCC phase amidst the FCC grains, from the remaining Liquid. Nonetheless, it is important to refer that the possibility for nucleation of each of these phases on the weld's microstructure is highly dependent, not only on the composition, but also on the temperature gradient and cooling rate. Furthermore, another major difference on the calculation results is the temperature solidification range of

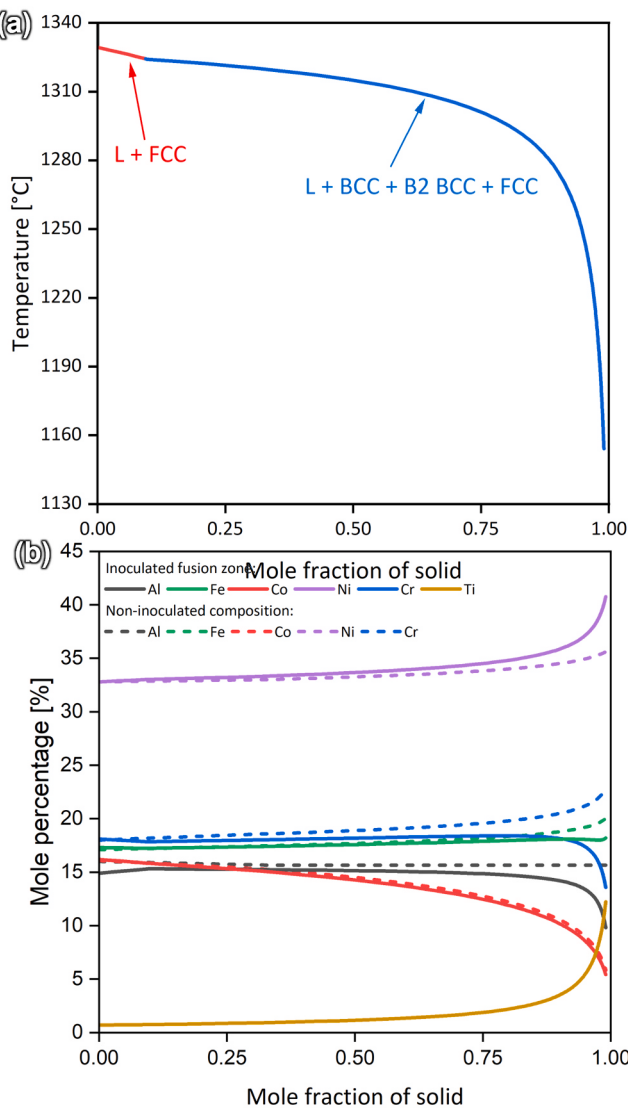


Fig. 8. – CalPhaD-based analysis of the phases formed during solidification using the Scheil-Gulliver method. The curve in (a) highlights the solidification path of the inoculated sample. Additionally, (b) shows the evolution of the composition in the liquid phase is shown for the non-inoculated and the TiB_2 -inoculated compositions.

each one: while for the BM, the Scheil model predicts a temperature range from 1333 to 1296 °C, in the non-inoculated and inoculated FZs vary between 1330°C and 1292°C and 1329°C and 1154°C, respectively. While minor composition changes induced by preferential evaporation led to minor changes in the solidification temperature range of the FZ (compared to the as-cast BM), the dissolution of Ti due to partial decomposition of TiB_2 promotes a significant change, which can lead to poorer weldability. However, despite the increasing solidification temperature range, which is often associated to higher probability for solidification cracking during welding, no such defects were found in the present joints.

From the Scheil-Gulliver calculations it is also possible to infer on the composition of the liquid phase during solidification of the molten pool. The variation of elemental distribution is displayed in Fig. 8(b). In the non-inoculated case, the Al content remains practically constant, while the Cr, Fe and Ni amounts tend to increase within the interdendritic fluid. Additionally, it is possible to observe that the amount of Co in the liquid decreases significantly. Therefore, such would allow us to infer that the interdendritic fluid would become richer in Cr, Fe and Ni, while

being depleted in both Co and Al. However, such is not the case of the FZ nor the BM (refer to Fig. 7(a) and Fig. 2(b), respectively), provided that the FCC phase, which solidifies first, is richer in Co, Cr and Fe, with the remaining Al and Ni elements being segregated to the remaining Liquid. Furthermore, in the inoculated case, Fe has the most stable evolution, while the content of Ni and Ti increases in the Liquid throughout solidification with the amount of Cr and Al decreasing in the final stages of solidification. The behavior of Co is similar to that observed in the non-inoculated case, which agrees well with the EDS map of Fig. 8(b), where the FCC (the first phase to form) showcases a higher content of Co.

Taking into consideration these CalPhaD-simulated microstructures both with and without TiB_2 added, further microstructure characterization using high energy synchrotron X-ray diffraction was performed. Representative diffraction patterns of the FZs of both conditions are detailed in Fig. 9.

Here it is possible to identify FCC and B2 BCC phases, including small intensity peaks corresponding to TiB_2 , and in some cases, we have overlapped phases, such as L_{12} and BCC with the FCC and B2 BCC

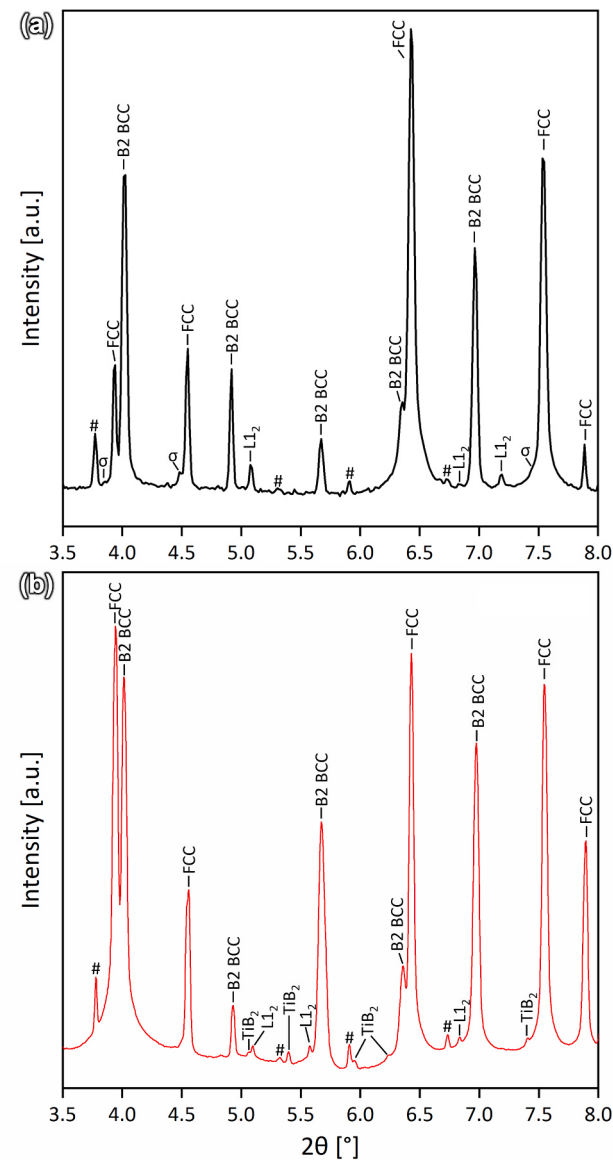


Fig. 9. – Representative synchrotron X-ray diffraction patterns of the FZ in: a) non-inoculated sample and b) in the TiB_2 -inoculated case. (# stands for the low intensity 2nd harmonic diffraction peaks that do not correspond to any structure present on the alloy).

phases, respectively. Interestingly, the identified phases are more compliant with equilibrium calculations than with the non-equilibrium Scheil calculations. The presence of TiB_2 diffraction peaks also confirms that full dissolution of the micron scale inoculant particles did not occur, which can then further improve the mechanical strength of the FZ.

The present section detailed the microstructure evolution along both joints, clarifying also the role of the TiB_2 particles on the as-solidified microstructure of the FZ. Given the distinct microstructure characteristic observed, it is conceivable that the local and macroscopic mechanical performance will be impacted. The next section assesses the mechanical behavior of the joints, correlating it with the observed microstructures.

4. Mechanical performance of the welded joints

4.1. Microhardness distribution

Beyond the discussed microstructural condition samples, the analysis of the mechanical behavior of the welds under mechanical solicitation is a measure that must also be considered for the evaluation of the microstructural influence on the behavior of the samples, whether imposed by the inoculation of the molten pool or not. As such, Fig. 10 exhibits the microhardness maps performed on both types of welded samples.

Comparing the microhardness maps from both samples it is possible to perceive that the in the non-inoculated sample the BM exhibit the higher values reaching $344 \text{ HV}_{0.5}$. Additionally, in both cases the HAZ exhibits similar values of microhardness, attaining a maximum of $283 \text{ HV}_{0.5}$, while the FZ is the region where most discrepancies exist, as expected due to the changes in microstructure observed. Regarding the non-inoculated sample, the FZ reached approximately $280 \text{ HV}_{0.5}$ at its peak, whereas in the TiB_2 -inoculated sample the same region reaches values up to $358 \text{ HV}_{0.5}$, as clearly indicated in Fig. 10 (b) and (c).

In this sense, it is possible to conclude that the introduction of TiB_2 affected the final condition of the samples resulting in a $\approx 28\%$ increase in hardness of the non-inoculated FZ values and $\approx 4\%$ increase when compared to the BM. This can be ascertained not only to the presence of the TiB_2 particles, acting as secondary phase strengthening, as well as

due the refined grain structure originated by the higher number of nucleation points associated to the presence of high temperature particles in the molten pool during welding.

4.1.1. Tensile behavior

To further inspect the weld mechanical behavior, stress-strains curves obtained on both types of welded samples are compared to the original BM as obtained by uniaxial tensile testing. These results are displayed in Fig. 11.

Starting by the tensile behavior of the non-inoculated joints, we can observe that the microstructural changes caused by the welding process, managed to improve the ultimate tensile stress (UTS) up to $1140 \pm 21 \text{ MPa}$ contrasting to those of the BM ($877 \pm 23 \text{ MPa}$). Nevertheless,

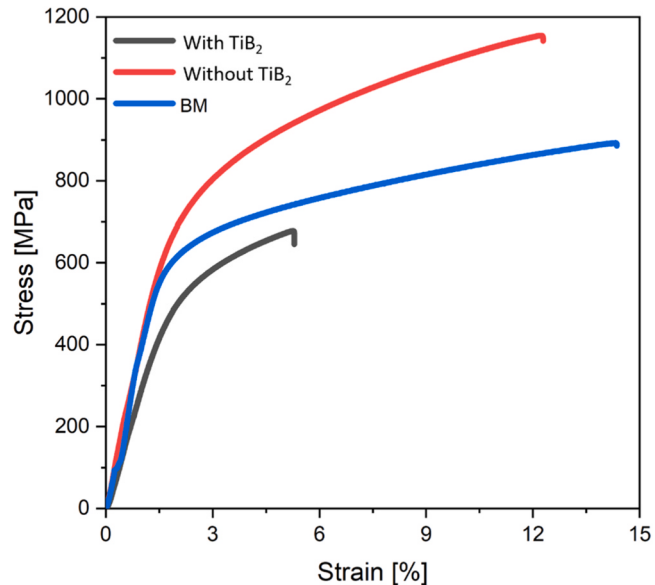


Fig. 11. – Representative tensile test results, showcasing the macroscopic mechanical properties of BM and welded joints.

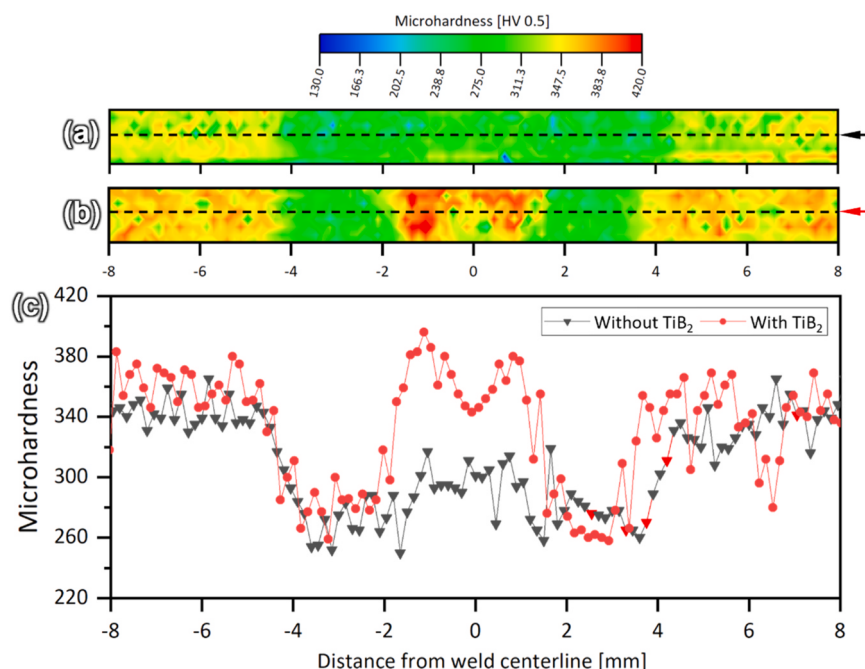


Fig. 10. – Microhardness distribution along the welded joint: a) microhardness map of the non-inoculated samples; b) microhardness map of the inoculated sample and c) microhardness distribution comparison at half height as indicated by the red and black arrow.

the strain to fracture is reduced from $12.1 \pm 0.3\%$ in the BM to $12.4 \pm 2\%$ in the non-inoculated material. Overall, the conventional welding procedure, i.e., without the use of TiB_2 in the FZ, promoted a $\approx 30\%$ increase in UTS and a decrease of $\approx 3\%$ in the strain to fracture. Nevertheless, one must consider that the highly dendritic nature of the BM is a key factor influencing its mechanical performance, as the smaller dendritic size attained on the FZ can help in improving the HEA's mechanical resistance. These results are in accordance with those observed in [21]. Nevertheless, the tensile test results on the inoculated sample indicate that despite the positive microstructural changes that occurred with the introduction of TiB_2 on the molten pool, the associated mechanical performance was diminished. Comparing the results with the BM the UTS of the inoculated samples ($667 \pm 15 \text{ MPa}$) showed a 63% decrease and the strain to fracture (corresponding to $4.6 \pm 0.9\%$) a 24% reduction. Eventually, both types of samples fractured in the HAZ/FZ interface.

Given the exhibited mechanical behavior, it is also of interest to understand the load partitioning between each region of the weld to evaluate how the strain is distributed during tensile testing as function of the different microstructure characteristics. For this, Fig. 12 a) and d) displays the DIC data corresponding to the regions corresponding to the BM, HAZ and FZ, in the moment right before fracture. Additionally, in Fig. 12 b) and e) it is possible to observe the time-resolved strain along the welded joints (where the stars mark the positions of interest analyzed).

From the DIC point analysis it is possible to observe the very different mechanical performance undertaken by each of the analyzed regions.

Firstly, in the non-inoculated welds we can observe a combined effort from the BM, HAZ, and FZ to accommodate the strain that is being applied upon the sample, with the BM displaying the most rigid behavior and the HAZ having the largest deformation. Such is expected from the microhardness exhibited by each region of the weld and can be correlated to the aforementioned effects of the weld thermal cycle on the observed microstructure.

In the TiB_2 -inoculated case, however, it is possible to observe that most of the strain is accommodated by the softer HAZ, while the FZ and the BM play a minor role in the deformation of the alloy. This phenomenon can be associated with the higher microhardness exhibited in these two regions, translating the higher strength performance of the FZ and the BM in comparison to the HAZ. Additionally, it must also be noted that compositional dissimilarity between the inoculated FZ and the non-inoculated HAZ can cause the generation of stress concentration areas to develop leading to premature failure of the weld. Moreover, the presence of the TiB_2 particles in the FZ can also act as stress concentrators further accelerating the material fracture. This suggests that the amount of TiB_2 added must be regulated to avoid excessive stress concentration effects, while grain refinement is still enabled by the particles.

Furthermore, one relevant information that is possible to take, is the fact the inoculated FZ is capable to sustain stresses up to $\approx 670 \text{ MPa}$ without any visible deformation, which in turn can sustain the premise for the development a new HEA composition with the possibility for high mechanical performance. Such, however, would require further analysis, which goes beyond the purpose of the present study.

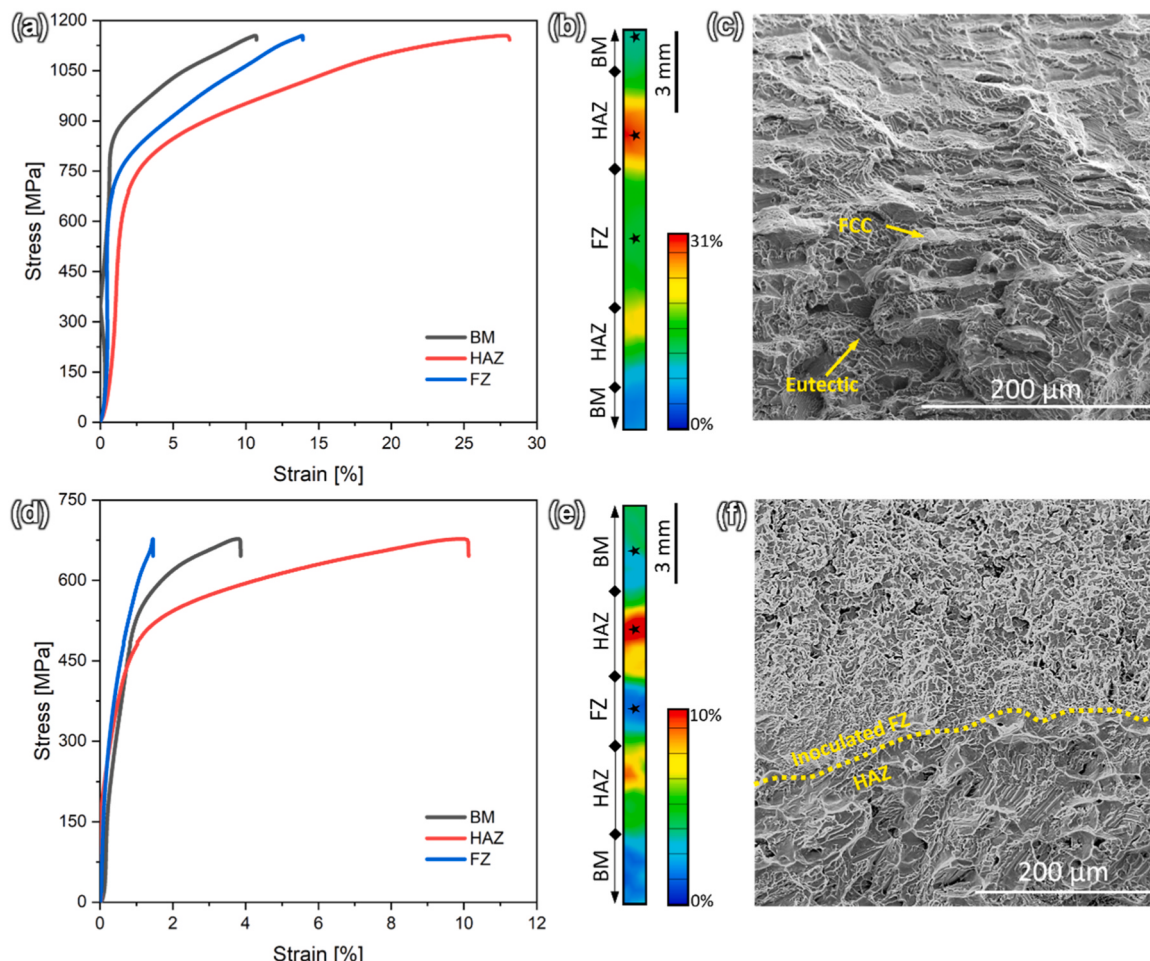


Fig. 12. – DIC point analysis obtained during tensile testing of: a) non-inoculated and d) TiB_2 -inoculated samples. Additionally, b) and e) exhibit the local strain distribution right before fracture of each sample. The fracture surfaces of the non-inoculated and inoculated samples are displayed in c) and f), accordingly.

In both cases, the HAZ is the region that exhibits the largest deformation, as it would be expected from microhardness mapping in Fig. 10, given the softening behavior of the HAZ which occurred during welding.

Given the eventual fracture of the samples during tensile testing, Fig. 12 c) and f) display the fractures surface of the inoculated and non-inoculated samples. It is possible to observe that in the non-inoculated case fracture occurred at the dendritic boundaries leaving traces of a composite-like FCC + Eutectic (FCC + B2 BCC) structures present on the surface. Such resulted from the combination of ductile and brittle fracture mechanisms arising from the presence of both phases on the microstructure. On the inoculated case however, it is possible to trace the discontinuity between the fracture surface resulting from the refined grain size of the FZ and the fracture surface arising from the HAZ microstructure. Such indicates that the interface between these two regions is critical to the inoculated weld performance.

5. Conclusions

This work delved on the investigation of the influence that TiB_2 particles have on the molten pool of GTAW welded plates of a AlCoCrFeNi HEA system. While defect-free welded joints were obtained, microstructural differences arising from the introduction of TiB_2 particles were evident. A distinct mechanical behavior of the inoculated and non-inoculated samples was observed, highlighting that the inoculation of the samples did not result in an improved mechanical condition of the HEA system, likely due to preferential stress concentration effects. Nevertheless, the results proved that tailoring the mechanical properties of GTAW welds on this HEA system is a possible procedure to be considered for potential engineering applications, as long as a correct selection of inoculant particles and their fraction is accomplished.

Overall, from this work the following topics can be assertively concluded:

- Excellent weldability via GTAW was observed on the AlCoCrFeNi HEA, where defect-free welds were obtained, both in the inoculated and non-inoculated condition.
- Grain size and phase fraction fluctuations allowed to observe the microstructural differences across the weld regions, where EBSD and conventional microscopy revealed a distinct phase distribution along the joints. The presence of a BCC phase in the TiB_2 -inoculated samples was unveiled by the Cr-rich regions on the corresponding FZ.
- Synchrotron X-ray diffraction was used to identify the phases present in the BM, HAZ and FZ of both types of samples. These being mainly composed of large FCC grains together with an eutectic constituent comprising a FCC and B2 BCC phases. Such phases were predicted via thermodynamic calculations, which allowed for a deeper analysis of the solidification path undertaken by both FZ during solidification.
- Considering the microhardness evolution, the BM exhibited the higher values in the non-inoculated samples. However, the higher microhardness values occurred in the inoculated sample's FZ, reaching up to 358 HV_{0.5}. Such values contrasted with the significantly softer FZ on the non-inoculated case (280 HV_{0.5}). In both cases the HAZ was the softer region of the joints.
- In terms of tensile behavior, in the as-welded condition, the best results occurred in the non-inoculated sample, which reached an UTS of ≈ 1140 MPa at a strain of $\approx 12\%$. The inoculated sample reached a UTS of ≈ 667 MPa (corresponding to $\approx 5\%$ of strain) indicating that the TiB_2 particles were not successful in improving the macroscopic mechanical properties of the BM. Both samples fractured in the HAZ.

Future works will envisage the application of different inoculants and fractions, as well as the use of different thermal treatments to optimize the mechanical properties of welded joints obtained from the AlCoCrFeNi HEA system.

CRediT authorship contribution statement

J.P. Oliveira: Writing – review & editing, Writing – original draft, Investigation, Formal analysis. **N. Schell:** Investigation. **R.S. Mishra:** Investigation. **P. Agrawal:** Investigation, Data curation. **J. Shen:** Investigation. **J G. Lopes:** Writing – review & editing, Writing – original draft, Investigation, Formal analysis, Data curation, Conceptualization. **A. Candeias:** Investigation, Formal analysis, Data curation.

Declaration of Competing Interest

The authors declare that they have no known competing financial interests or personal relationships that could have appeared to influence the work reported in this paper.

Data availability

Data will be made available on request.

Acknowledgments

JGL acknowledge Fundação para a Ciência e a Tecnologia (FCT - MCTES) for its financial support via the project UID/00667/2020 (UNIDEMI) and for funding the Ph.D. grant 2020.07350.BD. AC, JS and JPO acknowledges the funding by national funds from FCT - Fundação para a Ciência e a Tecnologia, I.P., in the scope of the projects LA/P/0037/2020, UIDP/50025/2020 and UIDB/50025/2020 of the Associate Laboratory Institute of Nanostructures, Nanomodelling and Nanofabrication – i3N. The authors acknowledge DESY (Hamburg, Germany), a member of the Helmholtz Association HGF, for the provision of experimental facilities. Beamtime was allocated for proposal I-20221211 EC. The research leading to this result has been supported by the project CALIPSOnplus under the Grant Agreement 730872 from the EU Framework Programme for Research and Innovation HORIZON 2020. The raw and processed data required to reproduce these findings cannot be shared as it forms a part of an ongoing study.

References

- [1] A. Parakh, M. Vaidya, N. Kumar, R. Chetty, B.S. Murty, Effect of crystal structure and grain size on corrosion properties of AlCoCrFeNi high entropy alloy, *J. Alloy. Compd.* 863 (2021) 158056, <https://doi.org/10.1016/J.JALLCOM.2020.158056>.
- [2] J. Zhu, S. Lu, Y. Jin, L. Xu, X. Xu, C. Yin, Y. Jia, High-temperature oxidation behaviours of AlCoCrFeNi high-entropy alloy at 1073–1273 K, *Oxid. Met.* 94 (2020) 265–281, <https://doi.org/10.1007/S11085-020-09991-6/FIGURES/14>.
- [3] Q. Tian, G. Zhang, K. Yin, L. Wang, W. Wang, W. Cheng, Y. Wang, J.C. Huang, High temperature deformation mechanism and microstructural evolution of relatively lightweight AlCoCrFeNi high entropy alloy, *Intermetallics (Barking)* 119 (2020) 106707, <https://doi.org/10.1016/J.INTERMET.2020.106707>.
- [4] K. Luo, G. Lei, S. Liu, C. Kong, H. Yu, Mechanical Properties and Microstructure Evolution of Cryorolled AlCoCrFeNi-Reinforced Aluminum Matrix Composites Tensile Tested at Room and Cryogenic Temperatures, (n.d.). (<https://doi.org/10.1007/S11661-023-07012-0>).
- [5] J.R. Deepak, R.P. Anirudh, S. Saran Sundar, Applications of lasers in industries and laser welding: a review, *Mater. Today Proc.* (2023), <https://doi.org/10.1016/J.MATPR.2023.02.102>.
- [6] V.P. Singh, R. Kumar, A. Kumar, A.K. Dewangan, Automotive light weight multi-materials sheets joining through friction stir welding technique: an overview, *Mater. Today Proc.* (2023), <https://doi.org/10.1016/J.MATPR.2023.02.171>.
- [7] J.F.S. Markanday, M.A. Carpenter, R.P. Thompson, N.G. Jones, K.A. Christofidou, S.M. Fairclough, C.P. Heason, H.J. Stone, Effect of NbC inoculants on the elastic properties and microstructure of additively manufactured IN718, *Materialia* 27 (2023) 101701, <https://doi.org/10.1016/J.MTLA.2023.101701>.
- [8] I.T. Ho, T.H. Hsu, Y.J. Chang, C.W. Li, K.C. Chang, S. Tin, K. Kakehi, A.C. Yeh, Effects of CoAl2O4 inoculants on microstructure and mechanical properties of IN718 processed by selective laser melting, *Addit. Manuf.* 35 (2020) 101328, <https://doi.org/10.1016/J.ADDMA.2020.101328>.
- [9] G.M. Grigorenko, L.I. Markashova, V.V. Golovko, E.N. Berdnikov, T.A. Alekseenko, V.V. Zhukov, Influence of titanium-containing inoculants on the structure of metal in the welds of high-strength low-alloy steels, *Mater. Sci.* 56 (2020) 195–202, <https://doi.org/10.1007/S11003-020-00415-Z/TABLES/4>.
- [10] Q.Z. Wang, X. Lin, N. Kang, X.L. Wen, Y. Cao, J.L. Lu, D.J. Peng, J. Bai, Y.X. Zhou, M. El Mansori, W.D. Huang, Effect of laser additive manufacturing on the microstructure and mechanical properties of TiB_2 reinforced Al-Cu matrix

- composite, Mater. Sci. Eng.: A 840 (2022) 142950, <https://doi.org/10.1016/J.MSEA.2022.142950>.
- [11] L. Xi, D. Gu, S. Guo, R. Wang, K. Ding, K.G. Prashanth, Grain refinement in laser manufactured Al-based composites with TiB₂ ceramic, J. Mater. Res. Technol. 9 (2020) 2611–2622, <https://doi.org/10.1016/J.JMRT.2020.04.059>.
- [12] M. Avateffazeli, P.E. Carrion, B. Shachi-Amirkhiz, H. Pirgazi, M. Mohammadi, N. Shamsaei, M. Haghshenas, Correlation between tensile properties, microstructure, and processing routes of an Al–Cu–Mg–Ag–TiB₂ (A205) alloy: Additive manufacturing and casting, Mater. Sci. Eng.: A 841 (2022) 142989, <https://doi.org/10.1016/J.MSEA.2022.142989>.
- [13] S.Y. Zhou, Y. Su, H. Wang, J. Enz, T. Ebel, M. Yan, Selective laser melting additive manufacturing of 7xxx series Al-Zn-Mg-Cu alloy: cracking elimination by co-incorporation of Si and TiB₂, Addit. Manuf. 36 (2020) 101458, <https://doi.org/10.1016/J.ADDMA.2020.101458>.
- [14] B. AlMangour, Y.K. Kim, D. Grzesiak, K.A. Lee, Novel TiB₂-reinforced 316L stainless steel nanocomposites with excellent room- and high-temperature yield strength developed by additive manufacturing, Compos B Eng. 156 (2019) 51–63, <https://doi.org/10.1016/J.COMPOSITESB.2018.07.050>.
- [15] S.C. Tjong, K.C. Lau, Abrasion resistance of stainless-steel composites reinforced with hard TiB₂ particles, Compos Sci. Technol. 60 (2000) 1141–1146, [https://doi.org/10.1016/S0266-3538\(00\)00008-7](https://doi.org/10.1016/S0266-3538(00)00008-7).
- [16] B. Zhang, G. Bi, P. Wang, J. Bai, Y. Chew, M.S. Nai, Microstructure and mechanical properties of Inconel 625/nano-TiB₂ composite fabricated by LAAM, Mater. Des. 111 (2016) 70–79, <https://doi.org/10.1016/J.MATDES.2016.08.078>.
- [17] Z. Zhang, Q. Han, Z. Liu, J. Gao, L. Wang, H. Liu, R. Wang, T. Ma, Z. Gao, Combined effects of heat treatment and TiB₂ content on the high-temperature tensile performance of TiB₂-modified Ni-based GH3230 alloy processed by laser powder bed fusion, Mater. Sci. Eng.: A 861 (2022) 144379, <https://doi.org/10.1016/J.MSEA.2022.144379>.
- [18] Y.L. Wang, L. Zhao, D. Wan, S. Guan, K.C. Chan, Additive manufacturing of TiB₂-containing CoCrFeMnNi high-entropy alloy matrix composites with high density and enhanced mechanical properties, Mater. Sci. Eng.: A 825 (2021) 141871, <https://doi.org/10.1016/J.MSEA.2021.141871>.
- [19] Z. Chen, X. Wen, W. Wang, X. Lin, H. Yang, Z. Jiang, L. Chen, H. Wu, W. Li, N. Li, Engineering fine grains, dislocations and precipitates for enhancing the strength of TiB₂-modified CoCrFeMnNi high-entropy alloy using laser powder bed fusion, J. Mater. Res. Technol. 26 (2023) 1198–1213, <https://doi.org/10.1016/J.JMRT.2023.07.244>.
- [20] J.G. Lopes, J.P. Oliveira, A short review on welding and joining of high entropy alloys, Metals 10 (2020) 212, <https://doi.org/10.3390/met10020212>.
- [21] J. Shen, P. Agrawal, T.A. Rodrigues, J.G. Lopes, N. Schell, Z. Zeng, R.S. Mishra, J.P. Oliveira, Gas tungsten arc welding of as-cast AlCoCrFeNi2.1 eutectic high entropy alloy, Mater. Des. 223 (2022) 111176, <https://doi.org/10.1016/J.MATDES.2022.111176>.
- [22] T.S.R.C. Murthy, J.K. Sonber, C. Subramanian, R.K. Fotedar, M.R. Gonal, A.K. Suri, Effect of CrB addition on densification, properties and oxidation resistance of TiB₂, Int. J. Refract Met. Hard Mater. 27 (2009) 976–984, <https://doi.org/10.1016/J.IJRMHM.2009.06.004>.
- [23] B.R. Golla, T. Bhandari, A. Mukhopadhyay, B. Basu, Titanium Diboride, Ultra-High Temperature Ceramics: Materials for Extreme Environment Applications 9781118700785 (2014) 316–360. (<https://doi.org/10.1002/9781118700853.CH13>).
- [24] J. Miao, H. Yao, J. Wang, Y. Lu, T. Wang, T. Li, Surface modification for AlCoCrFeNi2.1 eutectic high-entropy alloy via laser remelting technology and subsequent aging heat treatment, J. Alloy. Compd. 894 (2022) 162380, <https://doi.org/10.1016/J.JALLCOM.2021.162380>.
- [25] A. Lozinko, O.V. Mishin, T. Yu, U. Klement, S. Guo, Y. Zhang, Quantification of microstructure in a eutectic high entropy alloy AlCoCrFeNi2.1, IOP Conf. Ser. Mater. Sci. Eng. 580 (2019) 012039, <https://doi.org/10.1088/1757-899X/580/1/012039>.
- [26] I.S. Wani, T. Bhattacharjee, S. Sheikh, P.P. Bhattacharjee, S. Guo, N. Tsuji, Tailoring nanostructures and mechanical properties of AlCoCrFeNi2.1 eutectic high entropy alloy using thermo-mechanical processing, Mater. Sci. Eng.: A 675 (2016) 99–109, <https://doi.org/10.1016/J.MSEA.2016.08.048>.
- [27] D. Choudhuri, S. Shukla, P.A. Jannotti, S. Muskeri, S. Mukherjee, J.T. Lloyd, R. S. Mishra, Characterization of as-cast microstructural heterogeneities and damage mechanisms in eutectic AlCoCrFeNi2.1 high entropy alloy, Mater. Charact. 158 (2019) 109955, <https://doi.org/10.1016/J.MATCHAR.2019.109955>.
- [28] C.C. Tung, J.W. Yeh, T. tsung Shun, S.K. Chen, Y.S. Huang, H.C. Chen, On the elemental effect of AlCoCrCuFeNi high-entropy alloy system, Mater. Lett. 61 (2007) 1–5, <https://doi.org/10.1016/J.MATLET.2006.03.140>.
- [29] R.E. Reed-hill, PHYSICAL METALLURGY PWS-KENT, (2015). (<https://archive.org/details/physicalmetallur0000reed>) (accessed February 27, 2023).
- [30] S. Kou, Welding Metallurgy, Weld. Metall. (2002), <https://doi.org/10.1002/0471434027>.
- [31] Y.N. Hu, S.C. Wu, L. Chen, Review on failure behaviors of fusion welded high-strength Al alloys due to fine equiaxed zone, Eng. Fract. Mech. 208 (2019) 45–71, <https://doi.org/10.1016/J.ENGFRACMECH.2019.01.013>.
- [32] I. Cazic, J. Zollinger, S. Mathieu, M. El Kandaoui, P. Plapper, B. Appolaire, New insights into the origin of fine equiaxed microstructures in additively manufactured Inconel 718, Scr. Mater. 195 (2021) 113740, <https://doi.org/10.1016/J.SCRIPTAMAT.2021.113740>.
- [33] Y. Shao, X. Li, L. Chen, E. He, New insights into fine equiaxed zone of laser-welded 2A97 Al-Li alloy, J. Alloy. Compd. 895 (2022) 162717, <https://doi.org/10.1016/J.JALLCOM.2021.162717>.
- [34] L. Liu, T. Minasyan, R. Ivanov, S. Aydinyan, I. Hussainova, Selective laser melting of TiB₂-Ti composite with high content of ceramic phase, Ceram. Int. 46 (2020) 21128–21135, <https://doi.org/10.1016/J.CERAMINT.2020.05.189>.
- [35] J. Haidar, A theoretical model for gas metal arc welding and gas tungsten arc welding, I, J. Appl. Phys. 84 (1998) 3518–3529, <https://doi.org/10.1063/1.368527>.
- [36] J. Miao, H. Yao, J. Wang, Y. Lu, T. Li, Surface modification for AlCoCrFeNi 2.1 eutectic high-entropy alloy via laser remelting technology and subsequent aging heat treatment, (2021). (<https://doi.org/10.1016/j.jallcom.2021.162380>).
- [37] X.J. Wang, M. Xu, N. Liu, L.X. Liu, The formation of sigma phase in the CoCrFeNi high-entropy alloys, Mater. Res. Express 8 (2021) 76514, <https://doi.org/10.1088/2053-1591/ac0a5c>.
- [38] K. Kishore, S. Kushwaha, K. Sai, P. Teja, A.K. Chandan, M. Mukherjee, M. Adhikary, A. Kumar, Sigma phase embrittlement-induced failures of heat-resistant stainless steel traveling grate links, Eng. Fail Anal. 144 (2023) 106979, <https://doi.org/10.1016/j.englfailanal.2022.106979>.